

Star Grazing with Alumina Grass: Antireflection coatings in the visible and near-infrared on IPX-Clear Microlenses assisted by Grass-like Alumina

Ishan Rana^{a,b}, Suvrath Mahadevan^{a,b}, Megan Delamer^{a,b}, and Ceiwynn Longworth^{a,b}

^aDepartment of Astronomy & Astrophysics, Penn State, University Park , State College, USA

^bCenter for Exoplanets & Habitable Worlds, Penn State, University Park , State College, USA

ABSTRACT

Two-photon polymerization (2PP) enables the fabrication of high-precision micro-optics with complex freeform geometries, opening up a new parameter space for custom astronomical optics. Among the available resins, the newly developed IPX Clear is particularly well suited for visible applications, offering very high transmission rates across the visible and near-infrared spectrum, low surface roughness, and excellent shape fidelity. However, Fresnel reflections at the air–polymer interface introduce significant optical losses, which are detrimental in low-signal applications such as astronomy, where ever bigger telescopes are being built to collect more photons. Previous studies have found that grass-like alumina coatings on traditional glass and fused silica lenses improve average transmission from 91.9% up to 99% in the 400–900 nm spectral range. In our project, we explore the feasibility of Atomic Layer Deposition (ALD) for applying such a coating to IPX-Clear based micro-optics. In the 400–1700 nm range. Grass-like alumina based anti-reflective (AR) coatings can be designed to approximate the ideal refractive index for perfect destructive interference. This can be done by generating a gradual refractive index transition from air to the bulk IPX Clear substrate, suppressing surface reflections. While such grass-like coating has been demonstrated on bulk optics, and conformal ALD coatings have been applied to micro-optics built using 2PP. We demonstrate here—for the first time—the application of alumina grass coating to microlenses built using 2PP with the new IPX-Clear resin. In this study we have discussed the challenges and process steps of such applications. We observed Alumina grass coated micro lenses approximately lose 0.3% of photons due to reflection in the 400–850 nm range. In future work, we plan to test the performance of these microlenses in the entire 400–1700 nm range and explore methods to make coating more resilient, such as by applying an overcoat of SiO₂. The combination of these coating with the new and, highly optically transparent IPX-Clear resin opens up a regime of custom designed, highly efficient microlenses for various astronomical applications.

Keywords: Alumina Grass, IPX Clear, Atomic Layer Deposition, Anti-Reflective Coatings, Micro-optics

1. INTRODUCTION

1.1 Micro Optics

Micro-optics are widely used in astronomical instrumentation and telescopes, both ground- and space-based. A common use case is the Shack-Hartmann wavefront sensor¹ — an array of micro-lenses placed in front of a detector that track the gradient of a wavefront via centroid-shifting. This is a key element of adaptive optics (AO) systems implemented on the Keck 10 m telescopes^{2,3} and other ground-based optical facilities. Similar arrays of micro-lenses have also been incorporated into integral field spectrographs (IFS) like the Spectrographic Areal Unit for Research on Optical Nebulae (SAURON)⁴ on the William Herschel Telescope, or the VIRUS-2⁵ instrument on the McDonald 2.7 m telescope, as a way to feed an enlarged sky image into a multi-object spectrograph. IFS are incorporated into many subfields of astronomy, from galaxy evolution and dynamics to high contrast imaging of young stellar objects and their planetary systems. Some systems, like the Spectro-Polarimetric High-contrast Exoplanet REsearch (SPHERE) on the Very Large Telescope (VLT), contain multiple lenslet arrays

Further author information: (Send correspondence to Ishan Rana)

Ishan Rana.: E-mail: ikr5146@psu.edu

to combine extreme adaptive optics with the capabilities of an IFS.⁶ Micro optics have also been used in fiber double scramblers.⁷⁻⁹ Development work continues to create micro optics out of alternative materials such as silicon¹⁰ and find new ways to integrate lenses on small scales into photonic technology.¹¹

Two-photon polymerization (2PP)^{12,13} offers the possibility of utilizing complex freeform geometries on lenses smaller than those that can easily be produced through traditional optical manufacturing. The nature of 2PP also allows for precise placement of individual lenses relative to one another or relative to external markers, i.e., it does not necessitate the lenses be on the same underlying rectilinear grid or evenly positioned. The technique also enables scaling from R&D and prototyping to printing a number of microlenses, which led us to explore the use of this technique for coupling fiber from the Large Fiber Array Spectroscopic Telescope (LFAST)¹⁴ to its spectroscopic instrumentation. LFAST is a concept for a massively multiplexed array of telescopes, currently under development, that combines the light from many small apertures (0.76 m) into spectrometers. LFAST will operate in the 400-1700nm range. LFAST can achieve the sensitivity of a much larger telescope at a fraction of the cost of a traditional very large monolithic or segmented mirror. The LFAST fiber combiner uses an array of 19.2 μm high, 245 μm diameter, and 400 μm radius of curvature micro-lenses, Figure 1, placed directly over the center of the optical fibers to feed the light into a single square optical fiber.¹⁵

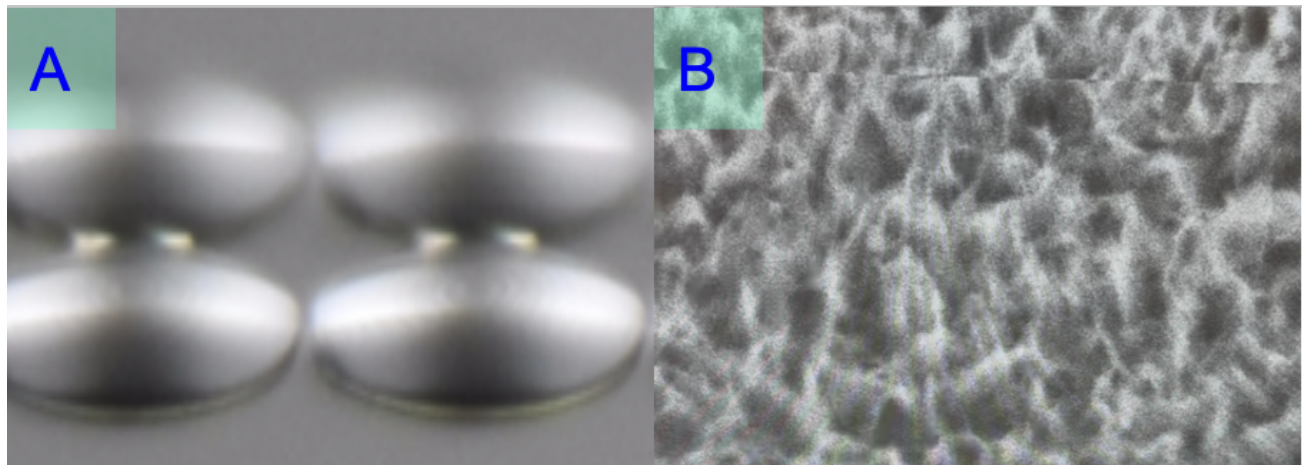


Figure 1. A) Side view of micro lenses being developed for the LFAST project, with diameter = 245 μm , radius of curvature = 245 μm and, height = 19.2 μm . Lens material is IPX clear, and Substrate is Fused Silica. B) SEM image of the Alumina Grass AR coating deposited on the surface of the micro lens. The coating is formed by depositing 35 nm of Alumina bloomed at 90° C for 10 minutes in DI water

1.2 Anti Reflective Coatings

Fresnel reflections from the micro-lenses can become a significant source of photon loss, something astronomers are especially sensitive to, given the cost of needing to build ever larger telescopes. To minimize this loss, we developed our micro-lens array using the newly developed and release IPX Clear resin from Nanoscribe*, which provides high internal transmission ($\sim 99.9\%$) in the visible and near-IR wavelength range. However, at the surface, due to reflections, $\sim 4\%$ of the photons are lost, which is essentially equivalent to losing 4% of the telescopes in the telescope array. It is therefore useful to further reduce these losses. The traditional way to address this is to apply a complex multilayer anti-reflective (AR) coatings to the microlens array, but the properties of the IPX-Clear resin precludes using very high temperature coatings.

AR coatings reduce reflection by matching the optical impedance between the incident medium and the substrate. This is done in two main ways.¹⁶

*Nanoscribe, “Photoresin IPX Clear” <https://www.nanoscribe.com/en/products/2pp-printing-materials/photoresin-ipx-clear-for-highly-transparent-microoptics/>.

(1) Deposited dielectric thin films: This method uses interference and/or admittance matching to drive the net complex reflection coefficient $r(\lambda, \theta)$ toward zero. In the admittance formulation, the AR condition is Equation (1),¹⁷ so the interface presents no mismatch to the incident wave.

$$Y_0(\theta) - Y_m = 0 \quad (1)$$

This implies that, to make a perfect AR coating using the dielectric layer method,

$$n_{AR} = \sqrt{n_{substrate} n_{air}} \quad (2)$$

$$d_{AR} = \frac{\lambda}{4n_{AR}} \quad (3)$$

For a perfect AR coating for IPX clear we would need a material with a refractive index of about 1.24 (Equation (2)), which does not exist in any bulk material. Also, single layer AR coatings are often narrow-band, but with addition of multiple layers it can be broadened.¹⁸ However, we do not wish to subject these lenses to the high temperatures or stresses required or resulting from complex multilayer dielectric AR coatings. Thus, this method is not ideal for LFAST micro-lenses.

(2) Sub-wavelength surface texturing: To develop AR coatings using this method, one can texture the surface to generate an effective graded-index layer $n_{eff}(z)$. Such a layer gradually transitions the impedance. AR coatings developed using this method can have effective refractive index in the 1.2 range¹⁶ (measured using ellipsometer), and such coatings are typically broadband,¹⁹ making it a promising method for use with IPX clear.

Near the top surface (the air interface), the effective refractive index (n_{eff}) is closer to that of air, and it gradually increases toward the dense material beneath until it reaches the refractive index of the original surface. To determine the gradient between refractive index at the surface and refractive index at the substrate, previous studies have used gaussian like fits.²⁰ In this study, we use an "Inverse bump function", A bump function is a gaussian like function which has the characteristic bell shape like the gaussian function but it terminates at a set point,

$$n(z) = n_{superstrate} + (n_{base} - n_{superstrate}) \sqrt{\frac{\ln(\frac{d}{z})}{\ln(\frac{d}{z}) + \alpha}} \quad (4)$$

Here $n(z)$ is the function that gives the effective refractive index at height z above the base of the gradient material. d is the effective height of the gradient material (can be measured using ellipsometer or be a fitting parameter), n_{base} is the refractive index of the gradient material at its base, $n_{superstrate}$ is the refractive index of the superstrate (in this case, air), and α is a fitting parameter that affects the width of the inverse bump.

We use the inverse bump function instead of an inverse gaussian function because the effective refractive index has a hard cut-off point at the base and at the air interface, i.e., refractive index there must be equal to that of original ALD Alumina layer and air, respectively.

In this paper, we demonstrate an AR coating solution for 2PP-fabricated micro-optics Section 1.1 using gradient refractive index effect of nanoporous amorphous alumina coatings and quantify the resulting improvement in throughput.

1.2.1 Atomic Layer Deposition

Traditional coating methods such as plasma-enhanced chemical vapor deposition,²¹ 3D printing of moth-eye type coatings,²² and ion-assisted electron beam evaporation²³ work well for creating coatings on simple surfaces, but they have limitations when used on complex surfaces such as multiple micro-optics or complex free form micro-optics.¹⁸ These techniques are largely directional and, therefore, cannot provide uniform coverage. For micro-optics like LFAST micro-lenses instead require conformal deposition methods like Atomic layer deposition (ALD).

ALD is a thin-film fabrication process that deposits atomic layers on a surface through self-limiting surface reactions.²⁴ In each cycle, the substrate is exposed to alternating chemical precursors that react only with surface

sites, producing highly uniform and conformal films even on complex, irregular structures. This makes ALD well suited for AR coatings on micro-optics. ALD has been used to deposit various single and multiple dielectric layers on micro-optic surfaces,^{18,25,26} demonstrating the proof of concept. In this work, we show that ALD techniques can yield high performance and broad-band (400-1700nm) AR coatings on IPX-Clear microlenses, making it suitable for astronomical applications.

1.2.2 Alumina Grass

Alumina Grass refers to the nano-porous structures that develop on the surface of ALD alumina after exposure to hot deionized (DI) water ($\geq 50^{\circ}\text{C}$).¹⁶ It is well established that alumina films can structurally transform in the presence of moisture and, in particular, during hot-water treatment,^{27,28} giving rise to these characteristic surface structures. Building on this corrosive behavior, some studies^{16,29-31} intentionally bloomed the resulting morphology to study its use as an AR coating on materials such as fused silica and D263 glass. The results were promising, with an average reflectance of 1% in the 350–800 nm range in Kauppinen et al.(2017),¹⁶ and $\leq 0.1\%$ in the 400-700 nm range in Guo et al. (2025).²⁹ We apply this technique to develop and characterize AR coatings to test on the LFAST micro-lenses.

2. BUILDING THE AR COATING

2.1 ALD Chamber

To build the AR coatings, we used the K.J. Lesker ALD 150 LE[†], a thermal ALD instrument at the Penn State Nanofabrication Facility. We deposit amorphous ALD alumina on the micro-lenses using the water-trimethylaluminum (TMA) process²⁴ at a chamber temperature of 80°C . We choose 80°C because alumina deposited at lower temperatures is less dense and has a lower effective refractive index (1.54). The value at this temperature is close to the refractive index of IPX Clear over our wavelength range of interest (400 nm to 1700 nm), which is desirable when there are no additional layers between the Alumina grass and IPX clear substrate. Figure 2 shows the change in refractive index with respect to ALD chamber temperature.

2.2 Blooming with DI Water

After ALD deposition, we treat the surface with deionized (DI) water to promote the growth of the nano-porous structures described in Section 1.2.2. This step transforms the smooth amorphous alumina into a porous, high-surface-area layer with a local packing fraction that varies with height. This resulting structure broadens AR performance and suppresses reflection across a wavelength band wider than a single abrupt interface.

2.2.1 DI Water Temperature

DI water temperature can affect the resulting “grass” morphology. In general, higher-temperature blooming produces a stronger anti-reflection effect because it promotes the formation of a more porous nanostructured layer on shorter timescales. A well-developed “grass” layer creates a smoother transition in effective index from air ($n \approx 1$) to dense alumina, which reduces Fresnel mismatch and suppresses reflection across a wider band. For this reason, many prior studies bloom alumina at temperatures $\sim 90^{\circ}\text{C} - 80^{\circ}\text{C}$, where the graded-index morphology forms reliably and yields improved reflectance outcomes^{16,29}. Figure 3 shows the reflection performance of 3 identical fused silica slides, coated with an identical ALD alumina layer (35 nm at 80°C) and bloomed at three different temperatures (50°C , 70°C , 90°C) for a set time (10 minutes).

We observe slides bloomed at high temperatures have better reflectance profiles. We also see that the slide bloomed at 50°C did not display any AR behavior. this is most likely due to the fact that the AR coating has not had enough time to fully bloom, although we note that in previous works,¹⁶ blooming was observed after 30 minutes of immersion in water at 50°C .

[†]<https://www.lesker.com/process-equipment-division/thin-film-systems/ald-150le-atomic-layer-deposition-ald-system.cfm>

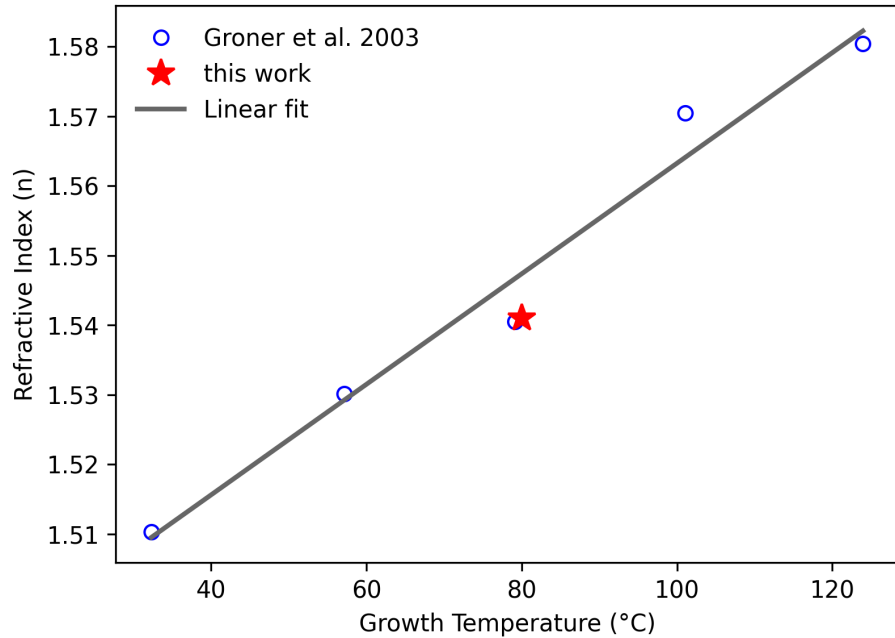


Figure 2. Change in refractive index of the alumina (y axis) with change in ALD chamber/Growth temperature (x axis). The data points are from.³² Here, we perform a linear fit to estimate the Alumina refractive index given a deposition temperature. We found the relation to be $n(T) = 1.48 + 7.96 \times 10^{-4}T$. This study also performed physical measurements using an ellipsometer (Red Star) for alumina deposited at 80°C. The results were nearly identical to previous work.³²

Table 1. Water quality measurements for Distilled vs Deionized Water.

Parameter	Distilled Water (Lab)	Deionized Water (NanoFab)
Resistivity (kΩ)	436	1740
TDS (ppm)	1.27	0.28
Alkalinity (ppm)	1.2	0.2
pH	7	0.5
ORP	360	120

2.2.2 Maintaining Sample Quality

For optimal results, it is essential to use high-quality deionized (DI) water (over $1M\Omega$ as measured in air) for blooming samples. Using lower-quality water, for example, lab distilled water, instead of DI water introduces dissolved ions and particulates that can dry into residues or streaks on the sample surface. This degrades optical performance by reducing transmittance and increases scattering. After blooming, we dry the samples with a nitrogen blow to remove residual droplets and minimize streak formation. The quality of DI water used to bloom samples in this work is summarized in Table 1, which shows the quality of DI water measured in the Penn State Nanofabrication facility and the distilled water measured in our lab using The Ultra-meter III™ 9P AHL Titration Kit.[†]

After blow-drying the samples with high purity nitrogen gas, some moisture may remain on the sample due to the amorphous nature of the alumina grass. Figure 4 shows dips in transmission around 1450 nm and 2200 nm, which coincide with well-known near-IR absorption bands associated with O–H species. The remaining moisture can be removed by treating samples in an oven at 85°C.²⁹

[†]Myron L® Company, “ULTRAMETER III™ 9P,” product page, <https://www.myronl.com/products/accessories-cases/ultrameter-iii-9p/>.

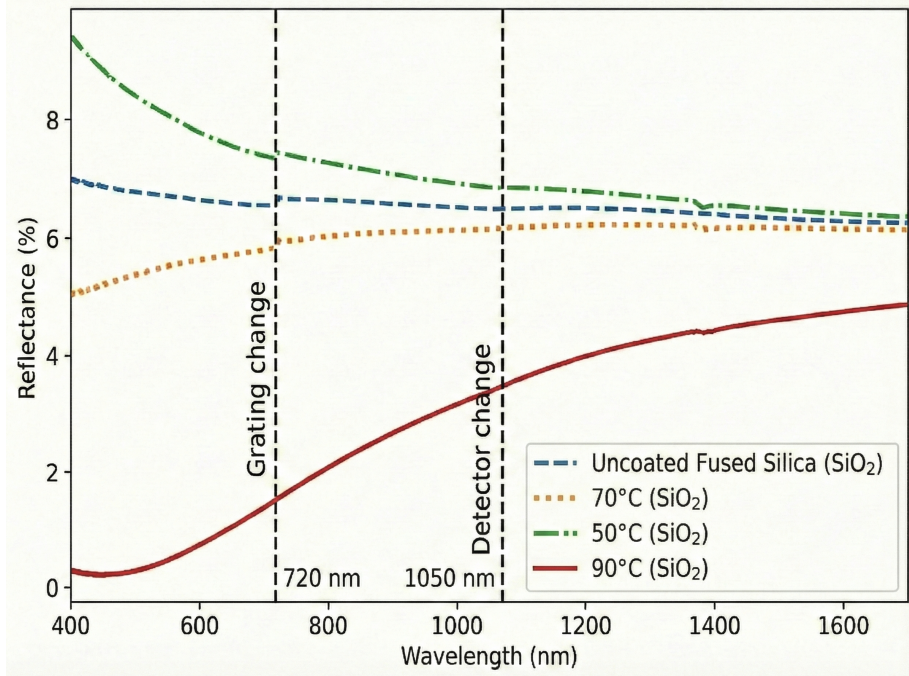


Figure 3. Reflectance% vs wavelength relation of an uncoated fused silica slide and 3 double sided ALD Alumina coated fused silica slides bloomed at different temperatures. All slides were coated with 35 nm of Alumina using ALD at a chamber temperature of 80°C. Each slide was then bloomed in a DI water bath for 10 minutes at 50°C, 70°C, and 90°C respectively. We then measure the Reflectance vs Wavelength relation of the bloomed slides and the uncoated slide. The slight kink observed at the ~ 700nm is due to grating change in the Carry 7000.

2.3 Simulations

Since the Alumina Grass layer optically behaves like a graded-index medium, we can simulate the performance of the coating using the transfer matrix method.³⁴ This is done by assuming a multilayer coating system where all layers have equal thickness (1 nm)¹⁶ and the refractive index of each layer is based on a unique $n_{\text{eff}}(Z)$ relation using Equation (4). This can be found by fitting the relation to the reflectance performance measured by spectrophotometer. Figure 5 shows the agreement of our fit to the measured reflectance profile of a double sided Alumina grass coating bloomed at 90°C and 35 nm ALD alumina layer.

We observe the fit agrees well with measured values for red/IR wavelengths average of 1.7% deviation. In Addition, the calculated height of AR coating was 150 nm, which is within the expected range. However, the fit does not perform well for blue wavelength range due to higher scattering. Other studies have encountered similar issues when fitting gradient profile in the blue wavelength regime¹⁶ due to scattering,

If the sample is thin, reflectance measurements of samples using a spectrometer will detect some reflections from the rear surface of the sample. Contributions from only the surface of the sample can be calculated using Equation (5), if both sides are identical (double side coatings) and assuming there is no internal transmission or scattering losses, i.e., Absorbance ~ 0 ³⁵

$$R = \frac{R_{\text{measured}}}{(2 - R_{\text{measured}})} \quad (5)$$

2.4 Combining Alumina Grass with Dielectric Method

To further broaden the anti-reflective effect across a wider wavelength range, we can add dielectric coatings ref Section 1.2 like silica (SiO₂) between the Alumina Grass and Substrate.²⁹ Figure 6 shows simulated results of a circle diagram illustrating how the addition of the underlying silica layer shifts the permittivity curve of

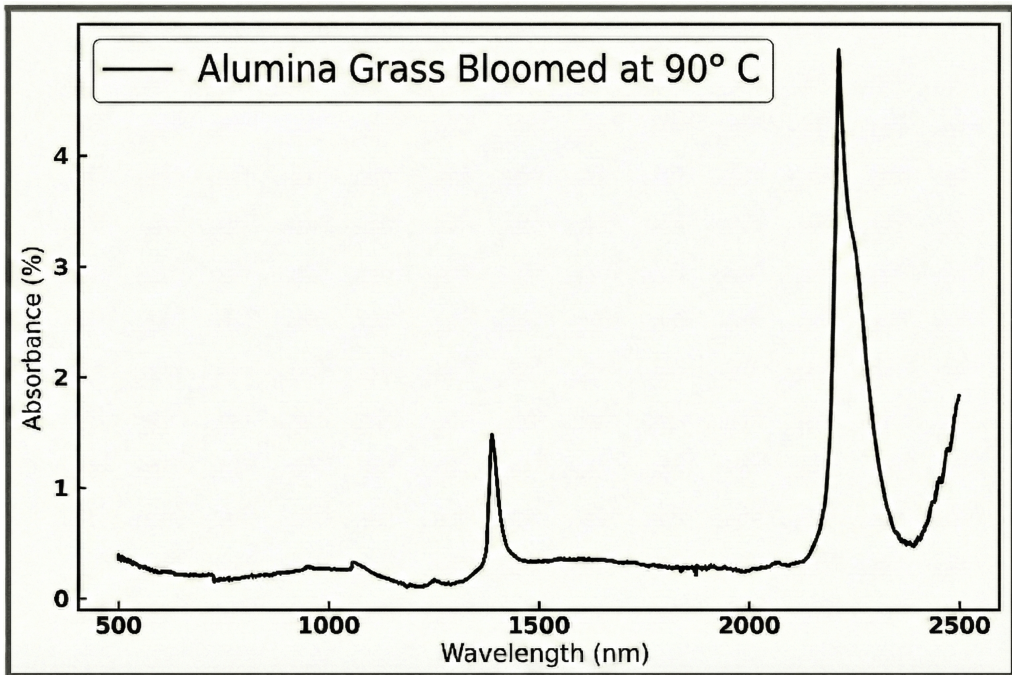


Figure 4. Absorbance% of a fused silica slide that was initially coated with 35 nm of alumina on both sides and then bloomed at 90°C. where $A = 1 - T - R$. Residual moisture on the AR coatings. We see two absorption features at $\sim 1390\text{nm}$ and $\sim 2200\text{nm}$, which indicates the presence of moisture. This can be attributed to the porous nature of alumina grass. To avoid this issue we suggest baking the samples after blooming. It is also been observed that blooming the samples in DI water for longer period of time reduces reflectance.³³

the sample. Figure 7 shows simulated results of how the thickness of the silica layer affects the reflectance curve of the sample. we observe that a 90 nm layer gives the best broadband effect as it is close to the quarter wave thickness.

3. PERFORMANCE OF ALUMINA GRASS

We measure the performance of the AR coating using the Agilent Cary 7000 UV-Vis-NIR spectrometer[§] and the Universal Measurement Accessory (UMA)[¶]. This spectrometer allows us to run a wavelength scan while maintaining a tightly defined geometry at a small angle (e.g., 6°). The UMA sets the sample angle precisely (0.02° resolution) and measures specular reflectance by placing the detector at twice the sample angle (i.e., 6° incidence and a 12° detector angle), which provides a repeatable “near-normal” specular reflectance spectrum.

3.1 Measuring Performance on Micro-optics.

The Agilent Cary setup has a minimum spot size of 2, mm \times 2, mm, which is much larger than the micro-lenses used in this study ($\sim 250, \mu\text{m}$). Therefore, we cannot directly use the spectrometer for these measurements. Instead, we use two different methods to extract the reflectance information.

[§]<https://www.agilent.com/en/product/molecular-spectroscopy/uv-vis-uv-vis-nir-spectroscopy/uv-vis-u-v-vis-nir-systems/cary-5000-uv-vis-nir?srsltid=AfmB0oor9cA1r9YrTQQcR7UA9XwXjf6Eokc101nlVS6X085c9SFi0BcI>

[¶]<https://www.agilent.com/en/product/molecular-spectroscopy/uv-vis-uv-vis-nir-spectroscopy/uv-vis-u-v-vis-nir-accessories/cary-universal-measurement-accessory-uma?srsltid=AfmB0opP9IAbCEZiZkXaJVXJXHOZiZ8OoseRKRidJpi59Sv0nmZCoMCq>

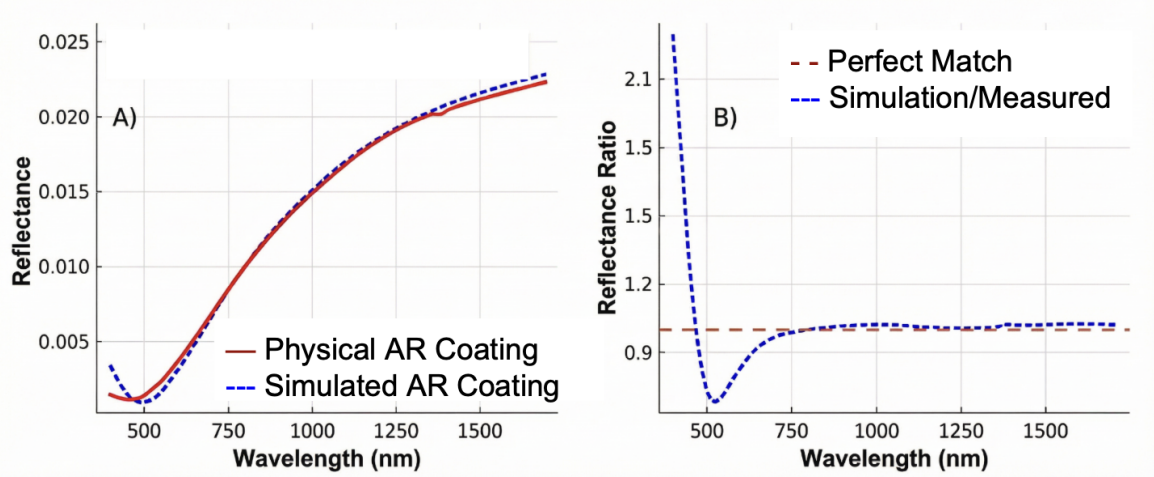


Figure 5. A) Back reflection separated Measured Reflectance (red) and Simulated Reflectance profile using optimized parameters of the bump function. B) Ratio of Blue over red curve from A). The Ratio is nearly one for IR and red wavelengths, while it deviates from 1 for blue wavelengths, indicating that the optimization yields an excellent match in the red and less so in the blue. This is likely due to scattering of blue light caused by the irregular structure of alumina grass, which is present in the data, but not accounted for in the simulations.

3.1.1 Method 1: Measure coating on different substrate and then model on IPX

In this method, we place a fused silica slide in the ALD chamber along with our samples. We keep the slide and the samples in the chamber at the same time to minimize differences in the AR coating. We then measure the reflectance versus wavelength curve using the Agilent Cary system and extract the graded profile of the coating using the method described in Section 2.3.

Using the extracted graded profile Figure 5, we simulate the reflectance and transmission versus wavelength for the microlenses by adding a base layer identical to that of the microlens in the simulation, in our case LFAST lenses can be approximated as a $250\mu\text{m}$ thick IPX Clear layer over a fused silica substrate. This yields the reflectance performance of the microlenses with the AR coating Figure 8.

3.1.2 Method 2: Relative reflection measurements on microlenses

For this method, we measure the reflected intensity, I_R , using the LabRAM Soleil Horiba confocal Raman microscope in micro-reflectance (micro-UV–Vis) (source is reliable up to 850nm). We illuminate the sample with a broadband source through the microscope objective, collect the reflected light from a selected region through the same objective (30° collection in this work), and send it to the spectrometer. The objective and confocal aperture set a $10\mu\text{m}$ spot size, which allows measurements on individual micro-optic features. However, this setup does not allow us to measure the total incident light, I_0 . Due to the highly anti reflective nature of our coating, the Raman spectrograph had to be set to 30° to be able to perform measurements.

Reflectance (R) is defined as

$$R = \frac{I_R}{I_0}. \quad (6)$$

Because we cannot directly measure I_0 , we instead use an identical uncoated micro-lens sample as a reference and perform the same measurement. This gives us the reflected intensity I_x . Using the AR-coated sample's reflected intensity I_{AR} and I_x , As shown in Figure 8 A we can compute the relative reflectance (R_{x-AR}) as,

$$R_{x-AR} = \frac{I_{AR}}{I_x}. \quad (7)$$

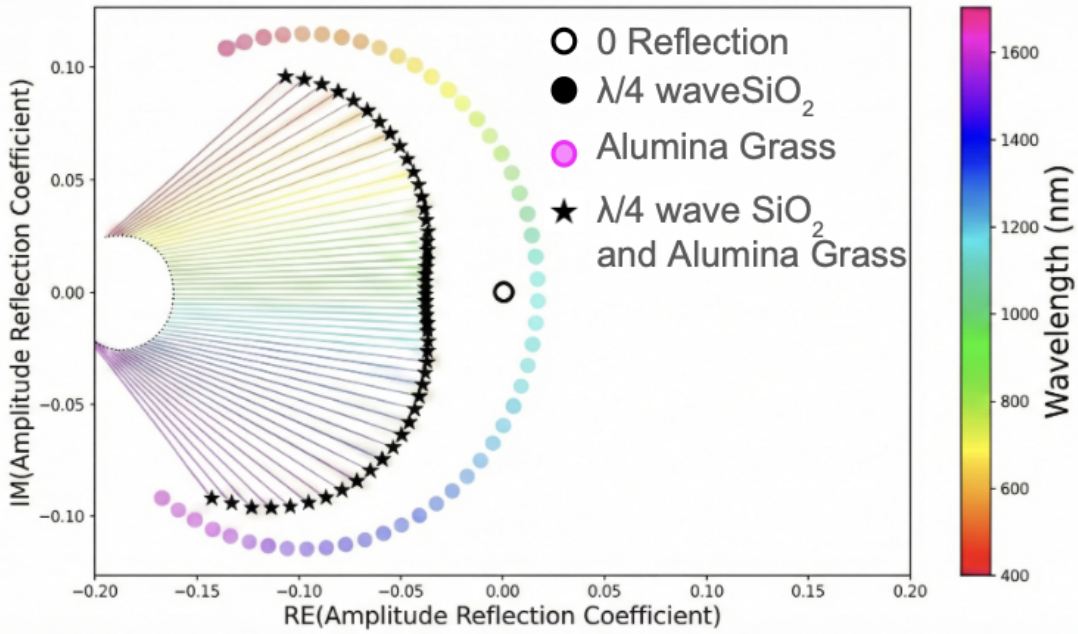


Figure 6. The following is a simulated modified circle diagram. Circle diagrams are typically used to track how the reflectance at a single wavelength changes as each layer is added to a multilayer coating; the final point on the plot gives the total reflectance of the full stack. Here, we apply the same idea across a wavelength range by plotting the terminal points for wavelengths from 400 nm to 1700 nm. We compare two systems. The first layer is a quarter-wave thick coating with refractive index 1.22, which is effective refractive index of our alumina grass samples bloomed at 90°C (Initial Alumina coating 35 nm). This layer is A) on a glass substrate of refractive index 1.55 and B) on a stack of 90 nm silica layer over glass substrate. The x- and y-axes represent the complex plane of the amplitude reflection coefficient. For each wavelength, the distance of the terminal point from the origin corresponds to the final reflectance at that wavelength. Points closer to the origin indicate lower reflectance and therefore better coating performance. We find that adding the silica underlayer flattens the wavelength-dependent curve and, overall, moves the terminal points closer to the origin. This reduces reflectance across a broader wavelength range, although it can increase reflectance at some wavelengths compared to the Alumina Grass alone.

The reflectance of the uncoated sample can then be calculated using R_x and the transfer matrix method,³⁴ treating the uncoated sample as a simple two-layer system Figure 8 B.

Since $R_x = \frac{I_x}{I_0}$, the absolute reflectance of the AR coating Figure 8, R_{AR} , is given by

$$R_{AR} = \frac{I_{AR}}{I_0} = \frac{I_x}{I_0} \times \frac{I_{AR}}{I_x} = R_x \times R_{x-AR}. \quad (8)$$

3.1.3 Comparing Method 1 and Method 2

Figure 8 C shows the reflectance profile for the AR coated microlenses using the two methods. Both methods show that the average reflectance is within 0.6% in the visible range, and the binned measurements are within 0.4%, indicating our coatings are highly anti-reflective. The average percentage deviation (binned) between the methods is 9% Figure 8 D.

4. DISCUSSION AND CONCLUSIONS

Our results show high coating performance across most of the wavelength band, with a slight trade-off at shorter wavelengths. With the SiO_2 underlayer and Alumina Grass, the effective thickness of the AR coating can be as

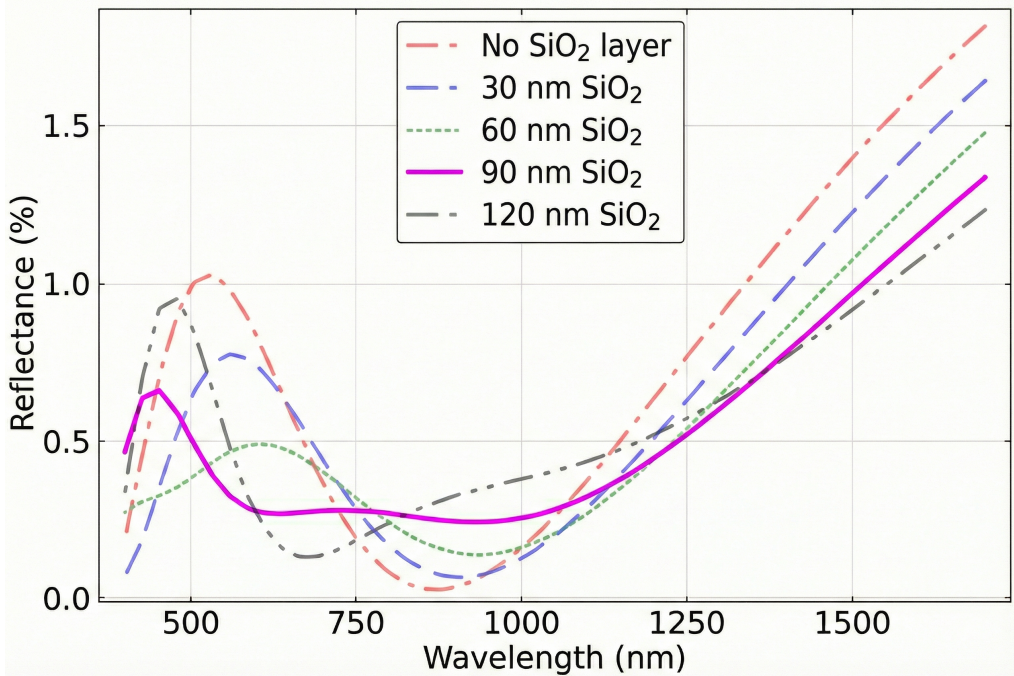


Figure 7. Simulation of Changes in the Reflectance profile of AR coated Soda-lime slides when an undercoat of fused silica is added between the coating and substrate. The addition of the fused silica layer broadens the reflectance profile, increasing reflectance at some points but overall reducing reflectance.

high as ~ 350 nm. therefore, we observe scattering at shorter wavelengths, which reduces the transmission in the UV-blue region.

The LFAST application also puts a constraint on the coating geometry. We can coat only one side of the lenses because the back side will be connected to silica optical fibers. If the AR coating is on the backside, it would rather reduce the transmission because the refractive indices of the fused silica substrate and the optical fibers are nearly identical.

Despite these constraints, this approach offers broad practical advantages. We are able to produce highly conformal and uniform coatings, and we can coat and bloom many samples in parallel. In future work, since alumina grass can degrade/corrode when exposed to moisture, A top coat of a water-resistant material such as silica or titanium dioxide²⁷ can be added over the AR layer to limit further corrosion from environmental exposure.

In this paper, we present an AR-coating approach for micro-optic arrays using atomic layer deposition and the anti-reflective behavior of hot-water-treated alumina. We use simulations to study how a graded-index coating and a SiO_2 underlayer broaden anti-reflective performance across a wider wavelength range. We also propose two measurement methods that quantify coating performance without requiring advanced nanoscale spectrometers. Together, these results provide a framework to design, model, and evaluate Alumina Grass AR coatings for micro-optic arrays under measurement and fabrication constraints. The development of such techniques will enable high efficiency bespoke and complex micro-optics for astronomical applications. d

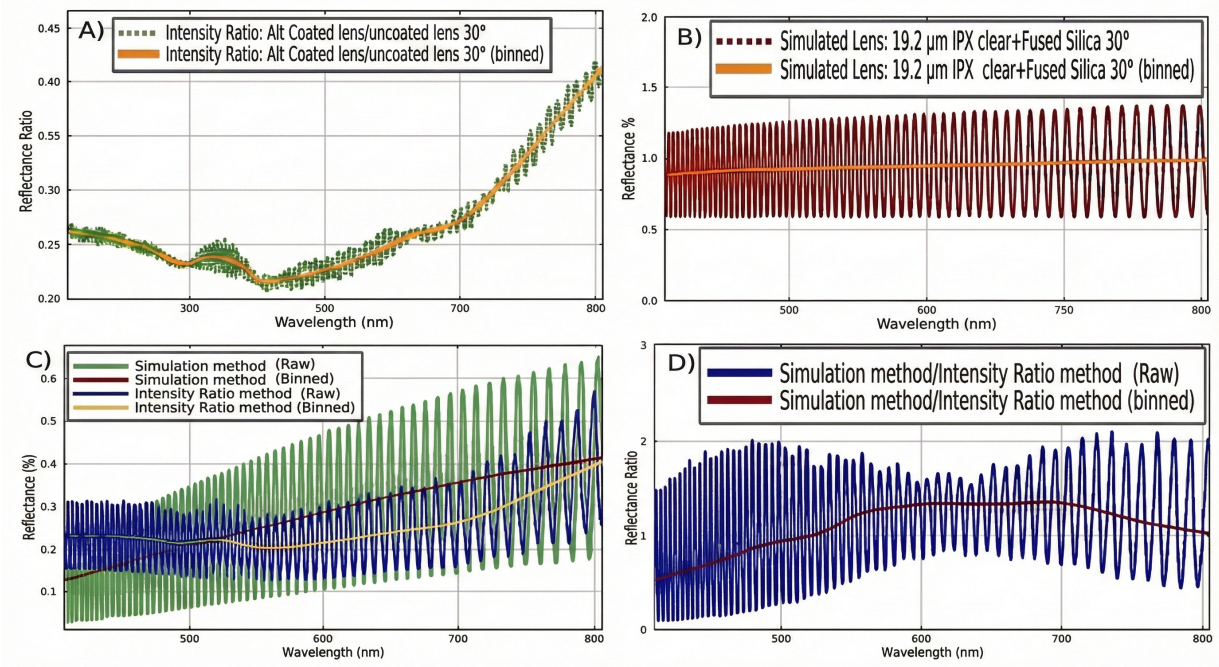


Figure 8. A) Intensity count ratio of AR coated lenses to Uncoated lenses (equivalent to Relative Reflectance). The Cyan graph shows the raw results and the red line shows the phase averaged result.
 B) Reflectance profile of a simulated Stack of $19.2\mu\text{m}$ IPX clear layer over Fused Silica (SiO_2) substrate. This is done to estimate the performance of the LFAST micro-lenses. The blue curve is the raw performance and the red curve is the binned performance.
 C) Reflectance of AR coated lenses calculated using Method 1 (Cyan and red) and Method 2 (Blue and Yellow)
 D) Ratio of Reflectance from Method 1 (Simulations) over Method 2 (Relative reflectance). The blue plot shows the raw data and the red plot shows the phase average results. The Ratio is within 1 ± 0.5 , indicating good agreement between the two methods.

ACKNOWLEDGMENTS

We acknowledge funding support from the Penn State Materials Research Institute for this program. The LFAST project is supported by Schmidt Sciences LLC. The Center for Exoplanets and Habitable Worlds is supported by the Pennsylvania State University, the Eberly College of Science.

REFERENCES

- [1] Platt, B. C. and Shack, R., "History and principles of shack-hartmann wavefront sensing," (2001).
- [2] van Dam, M. A. and Macintosh, B. A., "Characterization of adaptive optics at Keck Observatory," in [*Astronomical Adaptive Optics Systems and Applications*], Tyson, R. K. and Lloyd-Hart, M., eds., *Society of Photo-Optical Instrumentation Engineers (SPIE) Conference Series* **5169**, 1–10 (Dec. 2003).
- [3] Wizinowich, P., Chin, J., Correia, C., Lu, J., Brown, T., Casey, K., Cetre, S., Delorme, J.-R., Gers, L., Hunter, L., Lilley, S., Ragland, S., Surendran, A., Wetherell, E., Ghez, A., Do, T., Jones, T., Liu, M., Mawet, D., Max, C., Morris, M., Treu, T., and Wright, S., "Keck all sky precision adaptive optics," in [*Adaptive Optics Systems VII*], Schreiber, L., Schmidt, D., and Vernet, E., eds., *Society of Photo-Optical Instrumentation Engineers (SPIE) Conference Series* **11448**, 114480E (Dec. 2020).
- [4] Bacon, R., Copin, Y., Monnet, G., Miller, B. W., Allington-Smith, J. R., Bureau, M., Carollo, C. M., Davies, R. L., Emsellem, E., Kuntschner, H., Peletier, R. F., Verolme, E. K., and de Zeeuw, P. T., "The SAURON project - I. The panoramic integral-field spectrograph," *Monthly Notices of the Royal Astronomical Society* **326**, 23–35 (Sept. 2001).
- [5] Lee, H., Hill, G. J., Vattiat, B. L., Ramsey, J., Good, J., and Drory, N., "VIRUS-2 for the Harlan J. Smith telescope of the McDonald Observatory," in [*Ground-based and Airborne Instrumentation for Astronomy VII*], Evans, C. J., Simard, L., and Takami, H., eds., *Society of Photo-Optical Instrumentation Engineers (SPIE) Conference Series* **10702**, 107028E (July 2018).
- [6] Beuzit, J.-L., Vigan, A., Mouillet, D., Dohlen, K., Gratton, R., Boccaletti, A., Sauvage, J.-F., Schmid, H. M., Langlois, M., Petit, C., Baruffolo, A., Feldt, M., Milli, J., Wahhaj, Z., Abe, L., Anselmi, U., Antichi, J., Barette, R., Baudrand, J., Baudoz, P., Bazzon, A., Bernardi, P., Blanchard, P., Brast, R., Bruno, P., Buey, T., Carillet, M., Carle, M., Cascone, E., Chapron, F., Charton, J., Chauvin, G., Claudi, R., Costille, A., De Caprio, V., de Boer, J., Delboulb  , A., Desidera, S., Dominik, C., Downing, M., Dupuis, O., Fabron, C., Fantinel, D., Farisato, G., Feautrier, P., Fedrigo, E., Fusco, T., Gigan, P., Ginski, C., Girard, J., Giro, E., Gisler, D., Gluck, L., Gry, C., Henning, T., Hubin, N., Hugot, E., Incorvaia, S., Jaquet, M., Kasper, M., Lagadec, E., Lagrange, A.-M., Le Coroller, H., Le Mignant, D., Le Ruyet, B., Lessio, G., Lizon, J.-L., Llored, M., Lundin, L., Madec, F., Magnard, Y., Marteaud, M., Martinez, P., Maurel, D., M  nard, F., Mesa, D., M  ller-Nilsson, O., Moulin, T., Moutou, C., Orign  , A., Parisot, J., Pavlov, A., Perret, D., Pragt, J., Puget, P., Rabou, P., Ramos, J., Reess, J.-M., Rigal, F., Rochat, S., Roelfsema, R., Rousset, G., Roux, A., Saisse, M., Salasnich, B., Santambrogio, E., Scuderi, S., Segransan, D., Sevin, A., Siebenmorgen, R., Soenke, C., Stadler, E., Suarez, M., Tiph  ne, D., Turatto, M., Udry, S., Vakili, F., Waters, L. B. F. M., Weber, L., Wildi, F., Zins, G., and Zurlo, A., "SPHERE: the exoplanet imager for the Very Large Telescope," *Astronomy & Astrophysics* **631**, A155 (Nov. 2019).
- [7] Hunter, T. R. and Ramsey, L. W., "Scrambling Properties of Optical Fibers and the Performance of a Double Scrambler," *Proceedings of the Astronomical Society of the Pacific* **104**, 1244 (Dec. 1992).
- [8] Roy, A., Halverson, S., Mahadevan, S., and Ramsey, L. W., "Scrambling and modal noise mitigation in the Habitable Zone Planet Finder fiber feed," in [*Ground-based and Airborne Instrumentation for Astronomy V*], Ramsay, S. K., McLean, I. S., and Takami, H., eds., *Society of Photo-Optical Instrumentation Engineers (SPIE) Conference Series* **9147**, 91476B (July 2014).
- [9] Halverson, S., Roy, A., Mahadevan, S., Ramsey, L., Levi, E., Schwab, C., Hearty, F., and MacDonald, N., "An Efficient, Compact, and Versatile Fiber Double Scrambler for High Precision Radial Velocity Instruments," *Astrophysical Journal* **806**, 61 (June 2015).
- [10] Dahal, S., Stevenson, T. R., Costen, N. P., DeNigris, N., Glenn, J., Hu, G., Jhabvala, C. A., Morales-Sanchez, R., Patel, J. B., Quijada, M. A., Schrock, I., Wang, F. H., and Wollack, E. J., "Optimization of lenslet arrays for PRIMA Kinetic Inductance Detectors," *arXiv e-prints*, arXiv:2511.10773 (Nov. 2025).

[11] Arcadi, E., Douglass, G., Webb, J., Tremblier, G., Norris, B., Tuthill, P., Rossini-Bryson, S., Spalding, E., Martinod, M.-A., El Morsy, M., Lozi, J., Deo, V., Ahn, K., Vieuard, S., Guyon, O., Withford, M., and Gross, S., “Design, fabrication, and characterisation of a 3-baseline integrated optics beam combiner for nulling interferometry with simultaneous fringe tracking using tricouplers,” in [*Advances in Optical and Mechanical Technologies for Telescopes and Instrumentation VI*], Navarro, R. and Jedamzik, R., eds., *Society of Photo-Optical Instrumentation Engineers (SPIE) Conference Series* **13100**, 131002L (Aug. 2024).

[12] Goppert-Mayer, M., “Über elementarakte mit zwei quantensprungen,” *Ann. Phys.* **9**, 273–295 (1931).

[13] Maruo, S., Nakamura, O., and Kawata, S., “Three-dimensional microfabrication with two-photon-absorbed photopolymerization,” *Optics letters* **22**(2), 132–134 (1997).

[14] Bender, C. F., Angel, J. R., Berkson, J., Gray, P., Halverson, S., Kang, H., Kim, D., Monson, A., Oh, C. J., Rademacher, M., Schwab, C., Young, A., and Zaritsky, D., “The Large Fiber Array Spectroscopic Telescope: fiber feed and spectrometer conceptual design,” in [*Ground-based and Airborne Instrumentation for Astronomy IX*], Evans, C. J., Bryant, J. J., and Motohara, K., eds., *Society of Photo-Optical Instrumentation Engineers (SPIE) Conference Series* **12184**, 121844J (Aug. 2022).

[15] Delamer, M., Mahadevan, S., Bender, C., Longworth, C., Angel, R., Berkson, J., Choi, O. T. S., Gehoski, K., Monson, A., and Schwab, C., “POKEMON: print optimization for kilo-fiber experiments using micro-optics and nanostructures,” *arXiv e-prints* , arXiv:2509.00181 (Aug. 2025).

[16] Kauppinen, C., Isakov, K., and Sopanen, M., “Grass-like alumina with low refractive index for scalable, broadband, omnidirectional antireflection coatings on glass using atomic layer deposition,” *ACS Applied Materials & Interfaces* **9**(17), 15038–15043 (2017). PMID: 28398715.

[17] MACLEOD, H. A., [*Thin-film optical filters*], CRC PRESS (2021).

[18] Ristok, S., Flad, P., and Giessen, H., “Atomic layer deposition of conformal anti-reflective coatings on complex 3d printed micro-optical systems,” *Opt. Mater. Express* **12**, 2063–2071 (May 2022).

[19] Southwell, W. H., “Gradient-index antireflection coatings,” *Opt. Lett.* **8**, 584–586 (Nov 1983).

[20] Liu, L., Wang, X., Jing, M., Zhang, S., Zhang, G., Dou, S., and Wang, G., “Broadband and omnidirectional, nearly zero reflective photovoltaic glass,” *Advanced Materials* **24**, 6318–6322 (Sept. 2012).

[21] Angarita, G., Palacio, C., Trujillo, M., and Arroyave, M., “Synthesis of alumina thin films using reactive magnetron sputtering method,” *Journal of Physics: Conference Series* **850**, 012022 (June 2017).

[22] CLAPHAM, P. B. and HUTLEY, M. C., “Reduction of lens reflexion by the “moth eye” principle,” *Nature* **244**, 281–282 (Aug. 1973).

[23] Bhattacharya, R. S., Rai, A., and McCormick, A., “Ion-beam-assisted deposition of Al_2O_3 thin films,” *Surface and Coatings Technology* **46**(2), 155–163 (1991).

[24] Puurunen, R. L., “Surface chemistry of atomic layer deposition: A case study for the trimethylaluminum/water process,” *Journal of Applied Physics* **97** (June 2005).

[25] Astrauskytė, D., Galvanauskas, K., Gailevičius, D., Drazdys, M., Malinauskas, M., and Grineviciute, L., “Anti-reflective coatings produced via atomic layer deposition for hybrid polymer 3d micro-optics,” *Nanomaterials* **13**, 2281 (Aug. 2023).

[26] Cunha, F. M., Freitas, J. R., Pimenta, S., Silva, M. F., and Correia, J. H., “Silicon dioxide atomic layer deposition at low temperature for pdms microlenses coating,” *Optical Materials* **157**, 116167 (2024).

[27] Abdulagatov, A. I., Yan, Y., Cooper, J. R., Zhang, Y., Gibbs, Z. M., Cavanagh, A. S., Yang, R. G., Lee, Y. C., and George, S. M., “ Al_2O_3 and TiO_2 atomic layer deposition on copper for water corrosion resistance,” *ACS Applied Materials & Interfaces* **3**(12), 4593–4601 (2011). PMID: 22032254.

[28] Dokmai, V., Methaapanon, R., and Pavarajarn, V., “Corrosion of amorphous alumina in deionized water under mild condition,” *Applied Surface Science* **499**, 143906 (2020).

[29] Guo, X., Pesonen, L., Rönn, J., Leppilahti, L., Saarniheimo, M., and Sneck, S., “Ultra-antireflective optical coating with atomic layer deposition,” in [*Optica OIC — Optical Interference Coatings Conference 2025*], *Optica OIC — Optical Interference Coatings Conference 2025* , FB.2, Optica Publishing Group (2025).

[30] Kauppinen, C., Pasanen, T. P., Isakov, K., Serué, M., Heinonen, J., Vähäniemi, V., Lipsanen, H., and Savin, H., “Grass-like alumina coated window harnesses the full omnidirectional potential of black silicon photodiodes,” *Appl. Opt.* **60**, 10415–10420 (Nov 2021).

- [31] Isakov, K., Kauppinen, C., Franssila, S., and Lipsanen, H., “Superhydrophobic antireflection coating on glass using grass-like alumina and fluoropolymer,” *ACS Applied Materials & Interfaces* **12**(44), 49957–49962 (2020). PMID: 33084313.
- [32] Groner, M., Fabreguette, F., Elam, J., and George, S., “Low-temperature Al_2O_3 atomic layer deposition,” *Chemistry of Materials* **16**, 639–645 (02 2004).
- [33] Yang, Y., Cai, Q., Hu, E., Wang, K., Gao, M., Liu, B., Wang, S., Sun, X., Zhang, R., Duan, W., and Zheng, Y., “Porous alumina-based broadband anti-reflection film for optical absorption with superhydrophilic to superhydrophobic surface,” *Applied Surface Science* **690**, 162584 (2025).
- [34] Mackay, T. G. and Lakhtakia, A., [*The Transfer-Matrix Method in Electromagnetics and Optics*], Springer International Publishing (2020).
- [35] Look, D. C. and Leach, J. H., “On the accurate determination of absorption coefficient from reflectance and transmittance measurements: Application to fe-doped gan,” *Journal of Vacuum Science & Technology B, Nanotechnology and Microelectronics: Materials, Processing, Measurement, and Phenomena* **34** (June 2016).